Weather and Climate Extremes 54 (2026) 100969

Contents lists available at ScienceDirect

Weather and Climate Extremes

journal homepage: www.elsevier.com/locate/wace

Effects of microphysics and gray-zone convection on MCS organization: A case study of unprecedented extreme rainfall in South Korea

Dabeen Song [a], Xingchao Chen [b], Xiaoming Shi [c], Hanjie Shen [a], Daeun Kwon [d], Ga-Yeong Seo [d,e], Seung-Ki Min [d,*], Eun-Soon Im [a,c,**]

[a] Department of Civil and Environmental Engineering, The Hong Kong University of Science and Technology, Hong Kong, China
[b] Department of Meteorology and Atmospheric Science, The Pennsylvania State University, University Park, PA, United States
[c] Division of Environment and Sustainability, The Hong Kong University of Science and Technology, Hong Kong, China
[d] Division of Environmental Science and Engineering, Pohang University of Science and Technology, Pohang, South Korea
[e] K-water Research Institute, Daejeon, South Korea

ARTICLE INFO

Keywords:
Mesoscale convective systems
Extreme precipitation
Cloud microphysics
Gray-zone convection

ABSTRACT

Mesoscale convective systems (MCSs) embedded in quasi-stationary fronts are major drivers of extreme precipitation over South Korea, yet simulating their organization and rainfall structure remains challenging. This study investigates how cloud microphysics and gray-zone convective parameterization modulate MCS and non-MCS precipitation and the phase and amplitude of precipitation in an extreme event that recently occurred in South Korea. Using an optimized WRF-based Convection-Permitting Model (CPM) at 3 km grid spacing, we conduct eight sensitivity experiments combining two microphysics schemes (single-moment WSM6 and double-moment Thompson), each with and without the scale-aware convection schemes, plus additional experiments that modify key parameters controlling upper-tropospheric ice content. While all simulations reasonably reproduce the general pattern of extreme precipitation, they also exhibit systematic differences in peak location, intensity, and spatial extent of precipitation, along with contrasting MCS properties. The default WSM6 produces narrow, intense MCS precipitation cores and strong overturning that extends outside tracked MCS clouds. In contrast, ice-enhanced WSM6 and Thompson yield larger, more top-heavy systems with broader cold anvils and rainfall areas that better match observations. The impact of activating scale-aware convection schemes appears to be inconsistent across microphysics schemes, indicating a strong dependency on the accompanying microphysics configuration. These results demonstrate that, within the context of this extreme event, the choice of microphysics scheme and upper-level ice representation can regulate MCS organization, rainfall distribution, and vertical mass transport.

1. Introduction

Mesoscale Convective Systems (MCSs) are organized complexes of convective storms extending hundreds of kilometers and lasting several hours to more than a day (Houze, 2004, 2018). MCSs play a critical role in the global hydrological cycle, as they are responsible for more than half of total rainfall and frequently cause severe flood disasters in many regions (Feng et al., 2019; Hiraga et al., 2025). In South Korea, MCSs become particularly important during the summer monsoon season when they interact with quasi-stationary frontal boundaries, causing them to move slowly or even remain stationary (Kim and Lee, 2006; Jeong et al., 2016; Kim et al., 2025). This quasi-stationary behavior allows for self-reinforcing interactions in which new convective cells develop at the rear (back-building convection) while existing cells continue to move (training effect), resulting in intense and prolonged rainfall over localized areas (Schumacher and Johnson, 2005). Therefore, understanding the characteristics of MCSs is crucial for elucidating the physical mechanisms behind extreme precipitation. While the important role of MCSs in the vertical transport processes that influence the phase and amplitude of extreme precipitation is well documented (Chen et al., 2022), effectively simulating MCSs using numerical models remains challenging due to their complex nature. Addressing this issue

* Corresponding author. Division of Environmental Science and Engineering, Pohang University of Science and Technology, Pohang, South Korea.
** Corresponding author. Department of Civil and Environmental Engineering, The Hong Kong University of Science and Technology, Hong Kong, China.
E-mail addresses: skmin@postech.ac.kr (S.-K. Min), ceim@ust.hk (E.-S. Im).

https://doi.org/10.1016/j.wace.2026.100969
Received 7 February 2026; Received in revised form 26 August 2026; Accepted 23 October 2026
Available online 26 October 2026
2212-0947/© 2026 The Authors. Published by Elsevier B.V. This is an open access article under the CC BY-NC-ND license (http://creativecommons.org/licenses/by-nc-nd/4.0/).

requires a realistic representation of the multiscale interactions between convective dynamics and cloud microphysics (Fan et al., 2017). In this context, various attempts have been made to enhance the modeling of these atmospheric processes, leveraging recent advancements in computational capacity and a greater availability of observational data.

In Regional Climate Models (RCMs) with typical horizontal resolutions (10-50 km), convective processes have been parameterized within a grid (Prein et al., 2015). In this approach, sub-grid-scale convection is represented through empirical relationships based on bulk parameters of the surrounding atmospheric conditions. Furthermore, MCSs are neither explicitly resolved nor sufficiently parameterized. Therefore, the selection of a particular parameterization scheme can substantially influence the simulation, leading to significant uncertainty in model outputs (Randall et al., 2003; Hohenegger et al., 2008). Numerous studies have identified that such parameterized convection often underestimates the frequency and intensity of extreme precipitation events, resulting in systematic negative biases, particularly in short-duration extremes (Molinari and Dudek, 1992; Lenderink and van Meijgaard, 2008; Li et al., 2012). In response to these challenges, scale-aware convection parameterizations such as the Korea Institute of Atmospheric Prediction Systems' Simplified Arakawa-Schubert (KSAS) (Kwon and Hong, 2017), Grell-Freitas (Grell and Freitas, 2014) and the Multi-scale Kain-Fritsch (Zheng et al., 2016) schemes have been developed to dynamically adjust convective representations as a function of grid resolution. Moreover, great advancements in computational capacity in recent years have enabled the use of Convection-Permitting Models (CPMs) at finer grid spacing (<4 km), which explicitly resolve convective processes (Kendon et al., 2017; Fosser et al., 2020). CPMs have demonstrated considerable improvements in simulating extreme precipitation and mesoscale convective features. For instance, Fosser et al. (2024) reported that CPMs can substantially reduce the contribution of parameterization-related model uncertainties by more than 50%.

At convection-permitting resolutions where convection parameterization becomes unnecessary, which partially reduces the uncertainty associated with parameter settings, the direct impact of microphysics that determines the physical properties and vertical distribution of atmospheric hydrometeors grows significantly in modeling precipitation processes (White et al., 2017). Different microphysics schemes, including single-moment schemes (e.g., WSM6) that predict only hydrometeor mass and double-moment schemes (e.g., Thompson, Morrison) that predict both mass and number concentrations, produce fundamentally different representations of microphysical processes and their interactions with convective dynamics (Thompson et al., 2008; Morrison et al., 2009). Recent sensitivity studies have demonstrated that the choice of microphysics scheme significantly affects the characteristics of simulated MCSs and resulting precipitation (Wu et al., 2013; Huang et al., 2020). On the other hand, Feng et al. (2018) demonstrated that, despite producing similar precipitation patterns such as precipitation amount and diurnal cycle, Thompson and Morrison microphysics schemes produced markedly different MCS structural properties. In addition to scheme choice, key parameters within a microphysics scheme that define the properties of hydrometeors have direct control on simulated rainfall and convection structures. Because these parameters are usually diagnosed or prescribed as fixed values, their influence can vary across regions and precipitation phases (Lim, 2020; Kim et al., 2024). In particular, several studies have shown that the prescribed ice properties in microphysics schemes strongly modulate anvil ice water content and the microphysical structures of MCS clouds, including their horizontal extent and stratiform organization (Van Weverberg et al., 2013; Feng et al., 2018). These findings highlight not only that microphysics schemes strongly affect the cloud-precipitation structures of MCSs, but also that their impacts depend on how convective parameterizations feed moisture and hydrometeors into the convective regions, reflecting the close thermodynamic and microphysical coupling between cumulus and microphysics schemes in the model.

On the other hand, at 3-km gray-zone resolution, where convective drafts are only partially resolved by grid-scale dynamics, the coupling between cloud microphysics and scale-aware convection parameterizations becomes highly complex and non-linear. In this gray-zone regime, convection and microphysics schemes do not operate in isolation. Rather, they strongly interact through the exchange of resolved moisture, hydrometeors, and thermodynamic tendencies (Liu et al., 2018; Jeworrek and West, 2019). Convection schemes directly modulate the vertical profiles of sub-grid convective drying, heating, and the detrainment of cloud condensate into the resolved scales (Kwon and Hong, 2017). In turn, microphysics schemes govern the phase changes, conversions, and fall speeds of these hydrometeors, where diabatic heating and evaporative cooling alter the grid-scale vertical motion and moist static energy, thereby feeding back into the sub-grid convective triggering and mass flux (Jeworrek and West, 2019; Mishra et al., 2024). Consequently, jointly altering convection and microphysics configurations produces strongly non-linear responses in precipitation, hydrometeor partitioning, and cloud fields that cannot be explained simply by the sum of their individual effects (Qian et al., 2015; Liu et al., 2018). However, while previous studies have largely examined how microphysics and convection schemes separately influence precipitation sensitivity and convective organization, there remains a critical need to investigate their coupling effects and explicitly link them to the detailed structural organization and dynamics of MCSs that produce extreme rainfall.

Therefore, this study aims to fill this gap by explicitly investigating how the joint modulation of microphysics and scale-aware convection parameterizations shapes the structural organization of MCSs embedded in an extreme precipitation event over South Korea during August 8-11, 2022. This event, characterized by quasi-stationary MCSs that produced over 600 mm of rainfall in localized regions (KMA, 2023; Park et al., 2024), serves as an excellent testbed for modeling studies to examine the complex interplay between convective dynamics and cloud microphysical processes. To address this, we utilize a Weather Research and Forecasting (WRF)-based CPM with a 3 km grid spacing. This configuration has been optimized for simulating extreme precipitation in South Korea by tuning the domain size, spectral nudging technique, and physics settings (Kwon et al., 2025). Building on this, we conduct a series of sensitivity experiments configured with multiple combinations of convection representation and microphysics parameterizations. While Kwon et al. (2025) employed the WSM6 microphysics scheme, one of the most popular single-moment schemes (Hong and Lim, 2006), this study also includes the Thompson scheme (Thompson et al., 2008) as a double-moment option, which has shown significant performance in simulating MCSs in a previous study (Chen et al., 2021). Along with this, additional experiments with parameter adjustments in WSM6 and Thompson are conducted (see section 2.1). Furthermore, we conduct the experiments while turning on scale-aware convection schemes, KSAS and MSKF, which are reportedly effective in simulating precipitation in Korea and other regions (Kwon and Hong, 2017). This approach can enhance the experiment design, leading to more robust conclusions. Given that a 3 km resolution is still considered as the 'gray zone' (Prein et al., 2015), where convective processes are not fully resolved nor reliably parameterized, it remains an open question how incorporating scale-aware convection schemes with single-moment and double-moment microphysics schemes can influence the interactions between convective and cloud microphysical processes within our experimental framework. Indeed, some studies have demonstrated that retaining convection parameterizations at gray-zone resolutions remains beneficial for the representation of precipitation cores and intensity (Deng and Stauffer, 2006; Kwon and Hong, 2017; Stergiou et al., 2025). The analysis focuses on the characteristics of MCSs identified through a process-oriented cloud classification and tracking algorithm. Isentropic analysis is also employed to diagnose vertical mass transport characteristics, which may differ between MCS and non-MCS convection. Comparative assessments of varying capabilities derived from

different convection and microphysics settings allow for a deeper understanding of their impacts on MCS behavior and the performance in simulating precipitation. These findings could provide valuable insight into the key processes governing extreme precipitation simulations and establish useful benchmarks enhancing the performance of CPMs at gray-zone resolutions.

2. Method and data

2.1. Model configuration and experimental design

The Weather Research and Forecasting (WRF) model version 4.4 (Skamarock et al., 2019), a state-of-the-art regional climate and weather model, is employed in this study. The overall model configuration, including domain, resolution, and most physical parameterizations, follows a recent optimization study for extreme precipitation over South Korea (Kwon et al., 2025). The model domain is centered over South Korea and covers most of East Asia and the western North Pacific (Fig. 1). The simulations use a single domain with 3 km horizontal grid spacing and 50 vertical levels extending from the surface to approximately 50 hPa. Following Kwon et al. (2025), large-scale Spectral Nudging (SN) is applied to realistically represent the synoptic environment while allowing mesoscale systems to develop freely. SN is applied to the zonal and meridional wind components above the planetary boundary layer. The nudging coefficient is set to 0.0003 s^{-1} and is applied only to waves with wavelengths longer than approximately 1, 000 km. To capture the extreme precipitation event and the embedded MCSs, the WRF model is initialized at 00:00 UTC 1 August 2022 and integrated continuously through 16 August 2022, covering the development and evolution of this event. Initial and lateral boundary conditions are obtained from the ERA5 reanalysis (Hersbach et al., 2020) at 6-hourly intervals, provided by the European Centre for Medium-Range Weather Forecasts (ECMWF).

In Kwon et al. (2025), the WSM6 microphysics scheme along with a convection-permitting configuration was used. Here, the treatment of microphysics and convection is further diversified to examine the sensitivity of MCS characteristics to the model configurations. Two widely used microphysics schemes are employed: WSM6 (single-moment) and Thompson (double-moment). Each scheme is first run as a Convection-Permitting Model (CPM) without any scale-aware cumulus parameterization and then combined with scale-aware cumulus schemes, using either the KIAPS Scale-Aware Simplified Arakawa-Schubert (KSAS) or the Multi-Scale Kain-Fritsch (MSKF) scheme. This yields six primary experiments: WSM6_CPM, WSM6_KSAS, WSM6_MSKF, THOM_CPM, THOM_KSAS, and THOM_MSKF (Table 1).

Table 1
Summary of the eight sensitivity experiments designed for this study.

Simulation ID	Microphysics scheme	Description	Convection treatment
WSM6_CPM	WSM6	Default version of WSM6	Off
WSM6_KSAS	WSM6	Default version of WSM6	On (KSAS)
WSM6_MSKF	WSM6	Default version of WSM6	On (MSKF)
WSM6_CPMa	WSM6 (adjusted)	Same as WSM6_CPM, but accretion of ice by snow and ice fall speed are both reduced	Off
THOM_CPM	Thompson	Default version of Thompson	Off
THOM_KSAS	Thompson	Default version of Thompson	On (KSAS)
THOM_MSKF	Thompson	Default version of Thompson	On (MSKF)
THOM_CPMa	Thompson (adjusted)	Same as THOM_CPM, but the minimum size for the autoconversion of cloud ice to snow is doubled	Off

In addition, previous studies have shown that the default version of WSM6 tends to remove cloud ice too efficiently through rapid conversion to other hydrometeor species and fast fall speeds, which leads to an underestimation of anvil extent and upper-level ice content (Van Weverberg et al., 2013; Grasso et al., 2014). Based on these findings, in WSM6_CPMa, the accretion of ice by snow and the fallout speed of ice are both reduced by multiplying 0.5 to enhance the retention of upper-tropospheric ice. To achieve a similar effect in THOM_CPMa, we adjust the threshold diameter for the autoconversion of ice to snow. Studies have shown that such autoconversion size thresholds constrain and strongly affect upper-tropospheric ice and snow partitioning (Bao et al., 2019; Ko et al., 2022). Therefore, in THOM_CPMa, this threshold is doubled to allow a larger fraction of ice to remain in the upper troposphere.

By adjusting one or two parameters that control upper-level ice content, the vertical profiles of hydrometeors change, and the sensitivity of these changes depends on the microphysics scheme (Fig. 2). In WSM6, WSM6_CPMa shows a notable increase in the ice mixing ratio near 200 hPa compared with WSM6_CPM (Fig. 2j), whereas in Thompson the increase of ice from THOM_CPM to THOM_CPMa is much smaller (Fig. 2k), accompanied by a significant reduction in snow and an increase in cloud water. This indicates that a single-moment scheme, which diagnoses only mixing ratios, responds more directly to parameter adjustment than a double-moment scheme, which predicts both mass and number concentrations and involves more intricate interactions among different hydrometeor species.

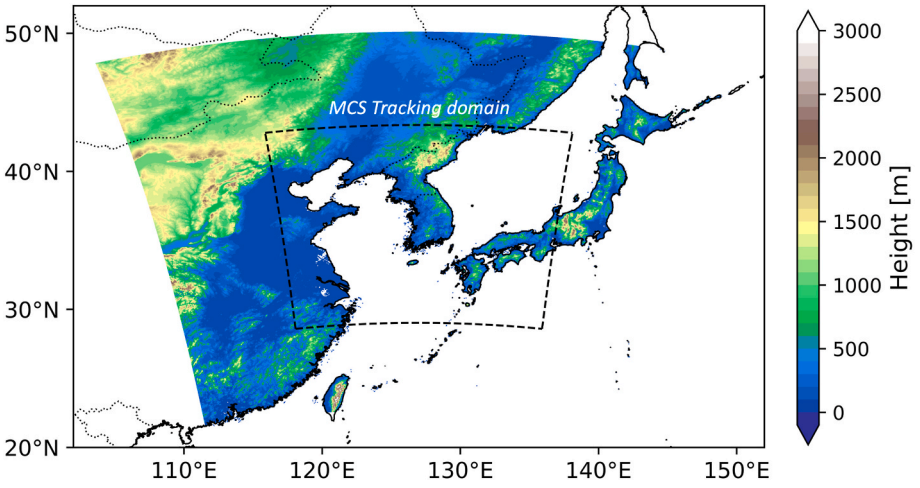


Fig. 1. Simulation and tracking domains. The colored area indicates the WRF simulation domain, and the black dashed box denotes the MCS tracking domain.

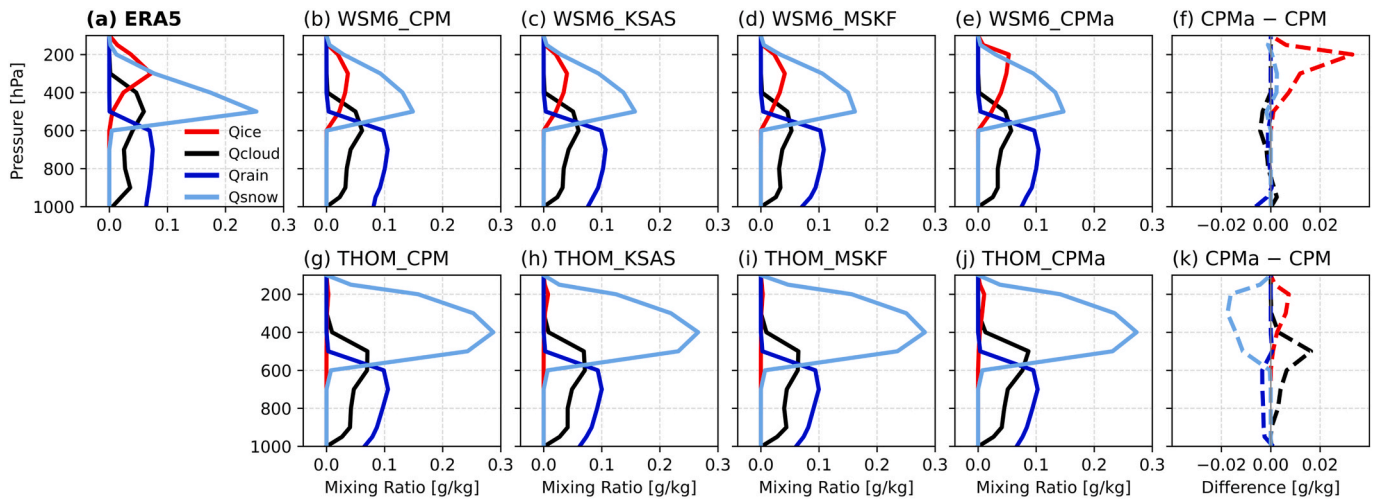


Fig. 2. Vertical profiles of hydrometeors simulated in different sensitivity experiments compared to the ERA5 reanalysis. For each hydrometeor, temporal and spatial averages are calculated from 8 to 10 August 2022 over the precipitation peak region spanning 35.5 °N to 38.5 °N and 125 °E to 130 °E. In each row, the rightmost panel represents the difference between CPMa and CPM for each microphysics scheme.

2.2. Case description

During 8-11 August 2022, South Korea experienced an extreme precipitation event driven by a quasi-stationary front that persisted for several days over the region. This event produced the highest cumulative rainfall record in recent years, with peak daily rainfall exceeding 400 mm in some regions and, causing widespread flood damage across the peninsula.

The synoptic-scale environment during this event highlights the meteorological conditions that favor the formation of MCSs and extreme rainfall (Fig. 3). Fig. 3a shows a narrow band of low cloud-top temperatures extending from eastern China into Korea, indicating that deep convection with organized cloud structures existed, which is a typical feature of mature mesoscale convective systems. These cold cloud tops reflect the strong updrafts and large vertical extent of the convective columns. Fig. 3b shows the large-scale thermodynamic and dynamic environment. The high equivalent potential temperature at 500 hPa aligned with the cloud band and a strong Vertically Integrated Moisture Transport (VIMT) exceeding 250 kg m^{-1} s^{-1} toward the peninsula created warm and moist conditions that were favorable for sustaining the MCSs.

2.3. MCS tracking algorithm

A process-oriented cloud classification and tracking algorithm is applied to identify and track convective systems in both observations and model simulations. We use PyFLEXTRKR (Feng et al., 2021, 2023), an object-based and flexible tracking framework that has been widely used to analyze the life cycle and structure of convective systems across different regions and datasets (Chen et al., 2023; Zhang et al., 2024; Tupsoundare et al., 2025). Tracking is performed over an 11-day period from 3 to 14 August 2022 to capture the full evolution of the 8-10 August extreme rainfall event.

The tracking workflow consists of three main steps. Cold Cloud Systems (CCSs) are first identified from hourly Brightness Temperature (T_b) fields, then linked in time to form continuous CCS tracks, and MCSs are finally determined as a subset of CCS tracks that meet additional cloud- and precipitation-based thresholds. A track is classified as an MCS if it (1) has a minimum cloud-shield area of 20,000 km^2, (2) contains at least one Precipitation Feature (PF) whose major axis exceeds 100 km, and (3) meets lifetime-dependent thresholds in duration (longer than 2 h), PF area, mean rain rate, rain-rate skewness, and heavy-rain fraction (>10 mm h^{-1}). The detailed algorithm and threshold criteria are

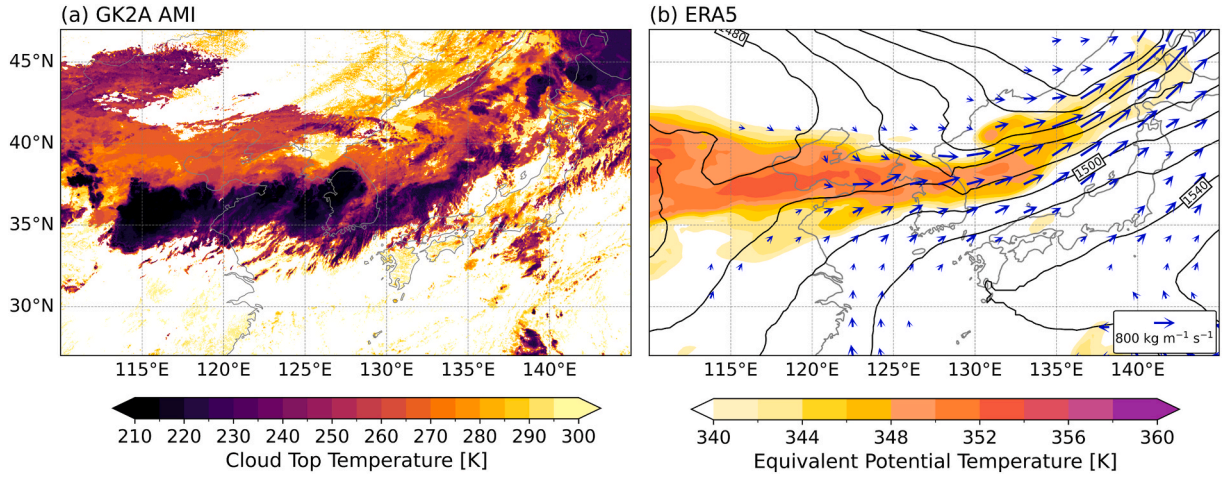


Fig. 3. Synoptic patterns at 03:00 UTC on 8 August 2022. (a) Cloud top temperature product is retrieved from the GEO-KOMPSAT-2A geostationary satellite's Advanced Meteorological Imager (AMI). (b) Equivalent potential temperature at 500 hPa (shading), geopotential height at 850 hPa (black contours), and VIMT (vectors) are taken from the ERA5 reanalysis dataset. Only VIMT values exceeding 250 kg m^{-1} s^{-1} are plotted.

described in Feng et al. (2023). In our study, the minimum cloud-shield area and duration were reduced from 40,000 to 20,000 km^2 and from 4 to 2 h, respectively. Because this event was driven by compact, narrow linear MCSs, these adjustments prevent the omission of the intense, localized systems that produced the extreme rainfall (Kim et al., 2025; Mun et al., 2025). Furthermore, such threshold tuning is highly recommended within the PyFLEXTRKR framework to properly capture the dominant convective modes of specific regions and cases (Feng et al., 2023).

2.4. Isentropic analysis

To examine how different convective systems redistribute mass in the vertical, an isentropic analysis is conducted following the framework by Pauluis and Mrowiec (2013) and Chen et al. (2018, 2022), 2022. In this approach, vertical mass fluxes are grouped according to the Equivalent Potential Temperature (EPT) of air parcels, so that atmospheric overturning is described in terms of height and EPT. Following Chen et al. (2022), the isentropic mass flux is decomposed into upward and downward motions using a two-stream approximation. This separates the upward transport of warm, moist air from the downward transport of cooler, drier air. These transports are computed separately for the convective and stratiform subregions of both MCS and non-MCS areas (using a 5 mm h^{-1} threshold; Tokay and Short, 1996) to evaluate how microphysics and convection treatments modify vertical mass circulation.

2.5. Evaluation metric for precipitation

The Fractions Skill Score (FSS) is employed to validate the model's performance in capturing precipitation. FSS compares the fraction of grid points exceeding a specified threshold within a surrounding spatial window between observations and simulations. In this study, a 9 km * 9 km neighborhood window (corresponding to 3 * 3 model grid points) is applied. FSS ranges from 0 (no skill) to 1 (perfect spatial agreement).

2.6. Observational data

In this study, the model's precipitation performance relative to observations is evaluated using the 500m high-resolution gridded precipitation dataset provided by the Korea Meteorological Administration (KMA 500m) and the Integrated Multi-satellitE Retrievals for GPM (IMERG) (Huffman et al., 2024). Both datasets are interpolated to the model resolution for a consistent comparison. The KMA 500m is produced based on station rain-gauge observations that are statistically downscaled into a very fine grid, providing detailed spatial information over land, and IMERG is a satellite-based global precipitation dataset developed as part of the Global Precipitation Measurement (GPM)

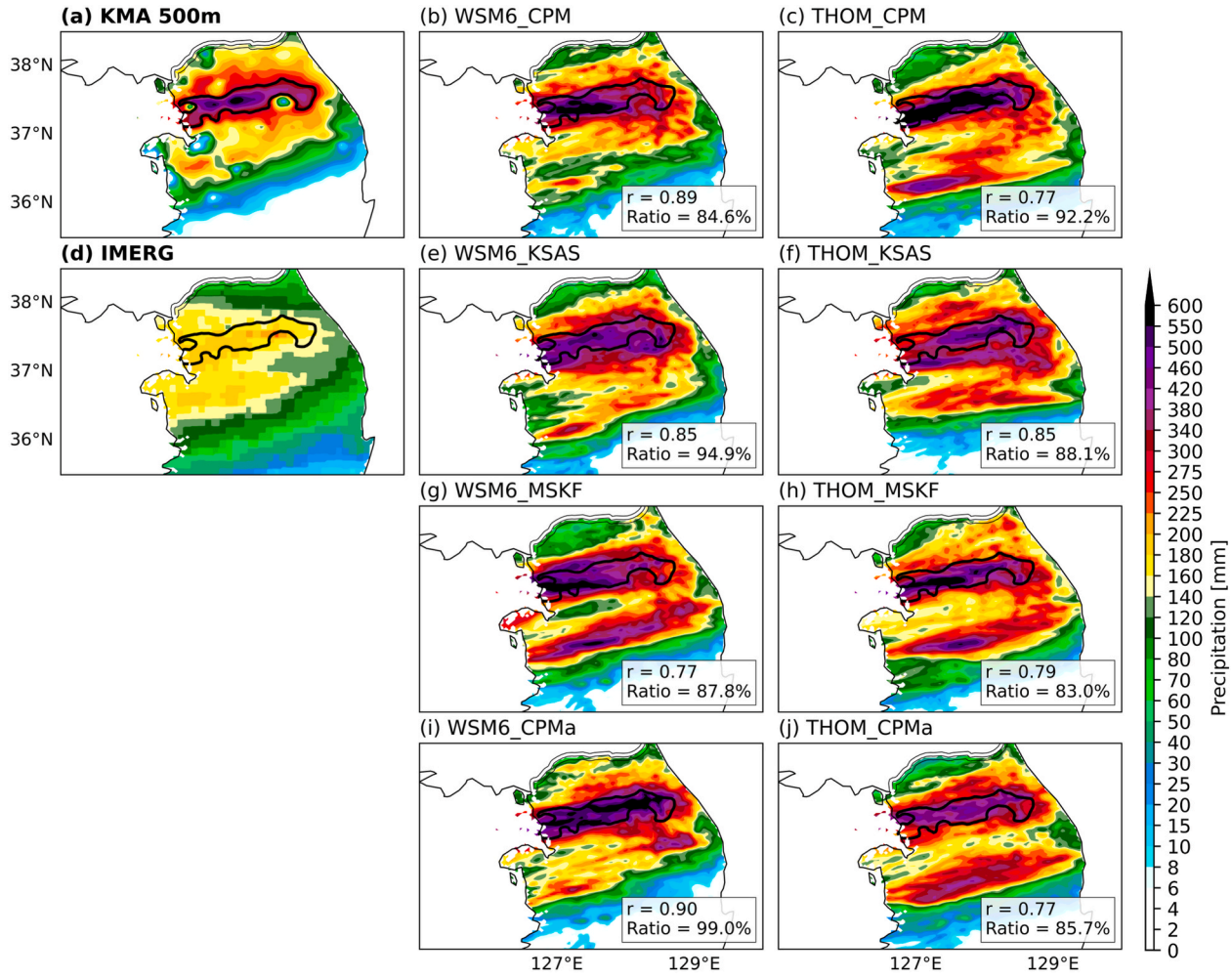


Fig. 4. Spatial distribution of precipitation accumulated from 8 to 10 August 2022 for each simulation. (a), (d) are observed precipitation from the KMA 500m and IMERG datasets, respectively. (b), (c), (e), (f), (g), (h), (i), and (j) are results from WRF simulations with different scheme settings. In each panel, the black contour is the outline of the area where KMA 500m precipitation exceeds 300 mm, r value in the lower-right corner indicates the spatial correlation with KMA 500m, and the ratio value is the fraction of model grids with precipitation exceeding 300 mm within the black outlined (observed) area.

mission led by NASA. Additionally, the ERA5 reanalysis is used to see the large-scale environmental patterns associated with the event.

For MCS tracking, two global satellite datasets are used. First, the cloud-top structure is characterized using infrared T_b from the NASA global merged geostationary product. Second, the precipitation data from IMERG are used together with T_b datasets to evaluate the simulated rainfall structure.

3. Result

3.1. Validation of simulated precipitation patterns

During 8-11 August 2022, all eight simulations reproduce the similar evolution (Fig. S1) and 3-day accumulated rainfall pattern to KMA 500m, but noticeable differences remain in the location and intensity of the core. Experiments using WSM6 (Fig. 4b, 4e, 4i) capture the main peak crossing the northern part of South Korea, whereas simulations using Thompson (Fig. 4c, 4f, 4h, 4j) and WSM6_MSKF (Fig. 4g) have a secondary peak farther south, which relatively lowers their spatial correlation (*r* values) with KMA 500m than WSM6. To quantify peak reproduction, we define a fraction ratio as the proportion of grid points within the observed peak area (3-day rainfall $\geq$ 300 mm) that also exceed 300 mm in each simulation. For WSM6, this ratio is lowest in WSM6_CPM and peaks in WSM6_CPMa, reflecting an improved east-west elongation of the rainband. Conversely, the ratio for Thompson gradually decreases from THOM_CPM to THOM_MSKF. These results indicate that microphysics choice primarily governs the number and placement of rainfall cores, whereas the convective parameterization mainly modulates the areal extent of extreme precipitation around them. Another notable difference arises from the core intensities between the two observational datasets (Fig. 4a and d). IMERG tends to underestimate precipitation magnitude over the core region, consistent with its known limitations capturing regional extreme rainfall (Da Silva et al., 2021; Zhu et al., 2022; Li et al., 2022). Despite this quantitative bias, the general spatial pattern of the accumulated rainfall in IMERG is broadly consistent with KMA 500m in a qualitative sense.

Over the 3-day period, the phase and magnitude of the rainfall band and related synoptic patterns vary markedly from case to case, as illustrated by two contrasting times in Fig. 5a and Fig. S4. Around 14:30 UTC on 8 August, a narrow but very intense rainband (hereafter referred to as the narrow case) produces a high local peak and modest total rainfall (Fig. 5b), whereas at 17:30 UTC on 9 August a broader, less intense convective system (hereafter referred to as the broad case) has lower peak intensity but much greater coverage and total accumulation (Fig. 5l). In these hourly snapshots, IMERG not only underestimates rainfall intensity but also places the precipitation core slightly farther south than KMA 500m (Fig. 5e and 5o), highlighting qualitative and quantitative discrepancies in hourly timescale that are less apparent in the 3-day accumulated fields. For the narrow case (Fig. 5b–k), KMA 500m shows that the mean precipitation intensity within the core area exceeds 29.5 mm h^{-1}, with the local maximum reaching up to 91.6 mm h^{-1}. Both WSM6_CPM and THOM_CPM reproduce this localized, intense rainband with comparable phase and magnitude, outperforming other configurations with the highest FSS values. In contrast, WSM6_KSAS, WSM6_MSKF, WSM6_CPMa, and THOM_MSKF generate an extended core farther south, whereas THOM_KSAS and THOM_CPMa displace the main core location and produce weaker rainfall within the observed core region.

These model differences are also evident in another hourly snapshot when the rainfall band has much broader coverage, as in the broad case at 17:30 UTC on 9 August. At this time, the rainfall band shifts slightly southward compared to the narrow case and extends meridionally over a much larger area, with a broader but weaker main core (Fig. 5l–u). In this broad case, CPMa and scale-aware cumulus schemes outperform the default CPM across both microphysics options (Fig. 5q and 5t). Conversely, the performance of the CPM configuration degrades notably in both schemes, as it produces a phase mismatch by placing the core outside the observed peak area or underestimates intensity, resulting in lower FSS values (Fig. 5m and 5n). In WSM6, activating the scale-aware cumulus schemes shifts the core toward the observed location with an expanded rain area, while WSM6_CPMa simulates a rain cell whose structure and intensity align closely with KMA 500m, reaching 8.5 mm h^{-1}. Similarly for Thompson, both scale-aware runs and ice-tuned run capture the broad core structure better than THOM_CPM. Although all simulations underestimate the observed intensity, these results suggest that the original CPM configuration better captures narrow, highly concentrated rainfall, while CPMa performs better for broader rainfall systems.

Consistent with the two contrasting hourly cases (Fig. 5), the FSS analysis across the top five sampled time-steps reveals a similar systematic dependence on rainfall regime, demonstrating that model skill varies substantially depending on whether the rainband is narrow and intense or broad and extensive. When evaluating the top five intense rainbands using rainfall intensity as the metric (Fig. 6a), the two default CPM configurations (THOM_CPM and WSM6_CPM) yield markedly higher FSS values than the other experiments, indicating that CPM runs generally demonstrate superior skill when localized rainfall is intense. Applying a lower threshold yields consistent results (Fig. S2). Notably, consistent with the higher skill of MSKF relative to KSAS seen in Fig. 5h and i, the two configurations using KSAS (WSM6_KSAS and THOM_KSAS) produce the lowest FSS values among all simulations.

In contrast, for broad rainbands (using total precipitation as a proxy for spatial extent; Fig. 6b), WSM6_CPMa substantially outperforms all other configurations. Unlike in WSM6, where WSM6_CPMa shows a marked improvement over other runs, THOM_CPMa yields only marginal differences compared with THOM_CPM, exhibiting nearly identical performance. Furthermore, compared to the variations observed across the WSM6 experiments, the four Thompson configurations, especially between THOM_CPM and THOM_CPMa, display much smaller differences among themselves, indicating limited sensitivity to both parameter tuning and convection parameterization. This tendency indicates that the microphysical parameter tuning has a much weaker impact on Thompson than WSM6. Physically, this difference stems from their representation of particle size distributions. The single-moment WSM6 scheme uses fixed intercept parameters for hydrometeors, making precipitation processes highly sensitive to direct tuning of ice-phase parameters (e.g., fall speed or size distribution constants). In contrast, the double-moment Thompson scheme independently predicts both the mixing ratio and number concentration of species like ice and rain. This likely allows the Thompson scheme to create a buffering effect where internal microphysical processes compensate for the manual parameter modifications, resulting in lower sensitivity to the tuning. Overall, this precipitation evaluation demonstrates that the choice of microphysics scheme exerts a greater impact than the convection treatment. Additionally, because the impact of activating the cumulus scheme is inconsistent across microphysics schemes, and the Thompson scheme shows limited sensitivity, the subsequent MCS analysis excludes the THOM_KSAS, THOM_MSKF, and THOM_CPMa configurations to focus on the experiments that demonstrate meaningful sensitivity in precipitation patterns.

3.2. MCS properties and sensitivity to microphysics adjustment

Although the rainfall-based evaluation clearly reveals differences in model skill and sensitivity to microphysical tuning, it does not elucidate the underlying physical mechanisms leading to the sensitivity. Therefore, we further analyze MCS properties using an object-based tracking framework and isentropic analysis. Despite IMERG's underestimation of rainfall intensity and phase discrepancies at hourly timescales compared to KMA 500m, it remains essential for MCS tracking analysis for several reasons. First, IMERG provides continuous temporal coverage over both land and ocean where gauge observations are not available. Second,

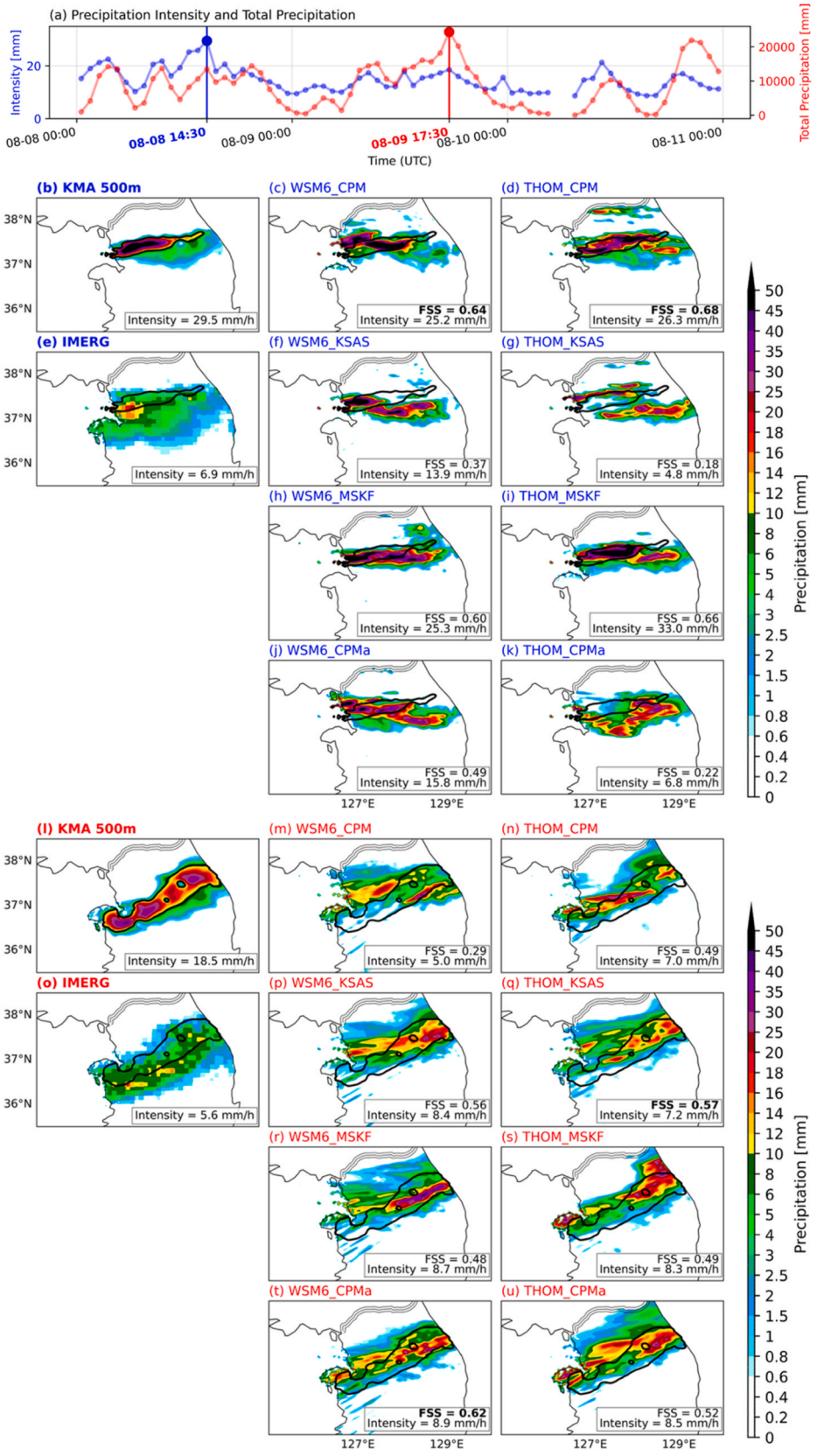


Fig. 5. Time series of precipitation intensity and total grid precipitation from the KMA 500 m, along with the spatial distribution of hourly precipitation at each peak for the simulations and observations. (a) Precipitation intensity (total precipitation) is calculated as the average (sum) of hourly precipitation over grid points where KMA 500 m precipitation exceeds 8 mm. (b)-(k) Spatial distributions of precipitation at the intensity peak at 2022-08-08 14:30 UTC. (l)-(u) Spatial distributions of precipitation at the total precipitation peak at 2022-08-09 17:30 UTC. In each panel, the black contour outlines the area where KMA 500 m precipitation exceeds 8 mm. The value in the lower-right corner indicates the Fractions Skill Score (FSS), with the best score in each column highlighted in bold, and Intensity denotes the mean precipitation within the KMA 500 m contour area. FSS is computed using a threshold of 8 mm and a 9 km * 9 km neighborhood window.

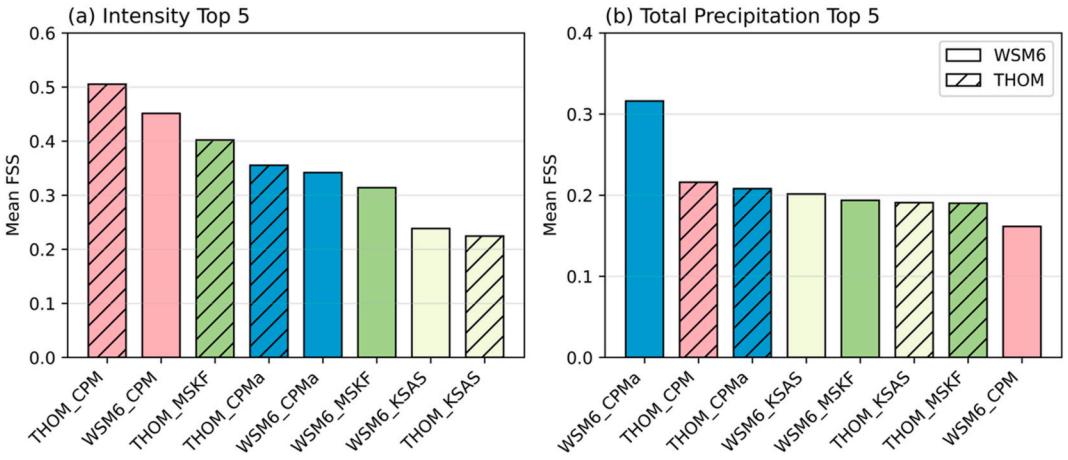


Fig. 6. Mean Fractions Skill Score (FSS) for each configuration for the top 5 intensity and total precipitation time-steps. The top five time-steps are selected based on (a) the highest KMA-observed precipitation intensity and (b) the highest KMA-observed total precipitation. FSS is computed using a threshold of 8 mm and a 9 km * 9 km neighborhood window.

combining IMERG with satellite-derived cloud-top brightness temperature (T_b) from the NASA merged geostationary product is a standard and well-tested approach in many previous studies. Thus, despite these limitations relative to station-based KMA 500m, its combination with geostationary T_b data provides a necessary observational basis for identifying, classifying, and tracking MCS clouds, and is well suited for the process-oriented evaluation performed in this study.

As shown in Fig. 5, the rainfall patterns during 8-10 August exhibit substantial case-to-case variability, with peak intensity and spatial coverage changing markedly. To examine how these contrasting rainfall structures are expressed in cloud-top and MCS properties, the tracking analysis first focuses on two distinctive examples: the narrow and broad cases. Fig. 7 illustrates how the choice of microphysics and its adjustment on the representation of cloud ice affect the cloud-top structures, precipitation, and MCSs in these two cases.

In the narrow case, the satellite observation shows an extensive region of cold cloud tops with most of the rainfall directly beneath it (Fig. 7b1, 7b2), whereas all simulations produce smaller, more fragmented cold cores. In this case, WSM6_CPM generates substantial precipitation outside the area of deep convection (Fig. 7c1, 7c2). In WSM6_CPMa, spatial agreement of precipitation with IMERG improves (Fig. 7f1, 7f2), with a single dominant precipitation feature, extending from the peninsula into the East Sea. Activating scale-aware cumulus schemes broadens both the convective cloud and rainfall band, and the main convective core becomes colder compared to CPM (Fig. 7d1, 7d2, 7e1, 7e2). THOM_CPM produces the widest cloud extent among the experiments, which is consistent with its own tendency to generate larger snow mixing ratio and anvil cloud shield.

In the broad case, where several small convective cores merge into a large cloud system (Fig. 7b3, 7b4), WSM6_CPM, WSM6_KSAS, and WSM6_MSKF do not reproduce the observed cold core within the tracked MCS region and locate the tracked MCS farther north compared to IMERG. However, WSM6_CPMa simulates a wider rain area whose structure and position follow the IMERG. This contrast reflects that the adjusted accretion of ice by snow and ice fall speed produces cold cloud shields that expand with the broader rain area, yielding larger MCSs that better match IMERG. Small stratiform regions are a known bias of the default WSM6 configuration, and previous studies have linked this behavior to its representation of ice and fast fall speeds, which enhanced convective precipitation while reducing stratiform areal coverage (Wu et al., 2013; Falk et al., 2019). The two snapshots therefore highlight that within WSM6, internal hydrometeor parameters that control upper-level ice and cloud extent show a stronger influence on representing MCSs than the choice between convection-permitting and parameterized settings. The original WSM6 with CPM configuration favors small, strongly developed cold clouds with substantial rainfall outside of the identified MCS, while WSM6_CPMa produces cold-cloud shields that expand with the broader rain area, yielding larger MCSs that better match the IMERG.

To place these two snapshots in a more comprehensive context, we next analyze the bulk structural and rainfall properties of all tracked MCSs. Fig. 8 summarizes the impact of the microphysics configurations on these bulk properties. In all simulations, MCS clouds are smaller than those identified from satellite observations, and the larger bias exists in WSM6_CPM, WSM6_KSAS, and WSM6_MSKF (Fig. 8a), indicating that activating scale-aware cumulus parameterizations in the convective gray-zone has only a marginal impact on MCS size (see also Fig. S3). MCSs in those simulations also have systematically warmer mean T_b (Fig. 8c) and higher mean rain rates (Fig. 8e) than in WSM6_CPMa and THOM_CPM, consistent with the small cold clouds and localized strong rainfall as seen in Fig. 7. These results show that the default WSM6 configurations favor very small, intensely precipitating cores while limiting the surrounding anvil area, thus simulating relatively warm and confined cloud shields. In contrast, the adjusted WSM6_CPMa and the Thompson scheme generate larger, more coherent MCS cores and more horizontally extensive cold anvils. For WSM6_CPMa, this enlargement of MCS area is accompanied by a notable decrease in core mean rain rate, indicating a transition toward broader, less concentrated convective structures that better match the observed MCS structure.

Besides the rainfall and cloud characteristics, we also examined the simulated underlying atmospheric overturning associated with MCSs using isentropic analysis (Fig. 9). Compared to the total mass transport in non-MCS regions (Fig. 9a2-9e2), MCSs exhibit much stronger vertical overturning (Fig. 9a1-9e1) and stronger downward mass transport below the melting level (~5.5 km), indicating stronger stratiform precipitation within MCS clouds. The vertical structure of MCS overturning differs among the experiments. WSM6_CPM, WSM6_KSAS and WSM6_MSKF have a primary peak near 10 km and an additional lower-level peak around 5 km. However, WSM6_CPMa and THOM_CPM show a single dominant peak at the upper levels, which clearly shows a 'top-heavy' MCS structure (Chen et al., 2022). The additional lower-level core in WSM6_CPM, WSM6_KSAS, and WSM6_MSKF is consistent with their stronger localized convective cores and may reflect stronger convective contributions despite less extensive MCS cold anvils. Another notable difference appears outside the MCSs. Among the simulations, WSM6_CPM produces the strongest vertical overturning in non-MCS regions, suggesting that convective activity and precipitation features extend beyond the MCS boundaries. This behavior is consistent with Fig. 7, where WSM6_CPM produces additional precipitation cores outside the main cold cloud shield, implying that part of the extreme

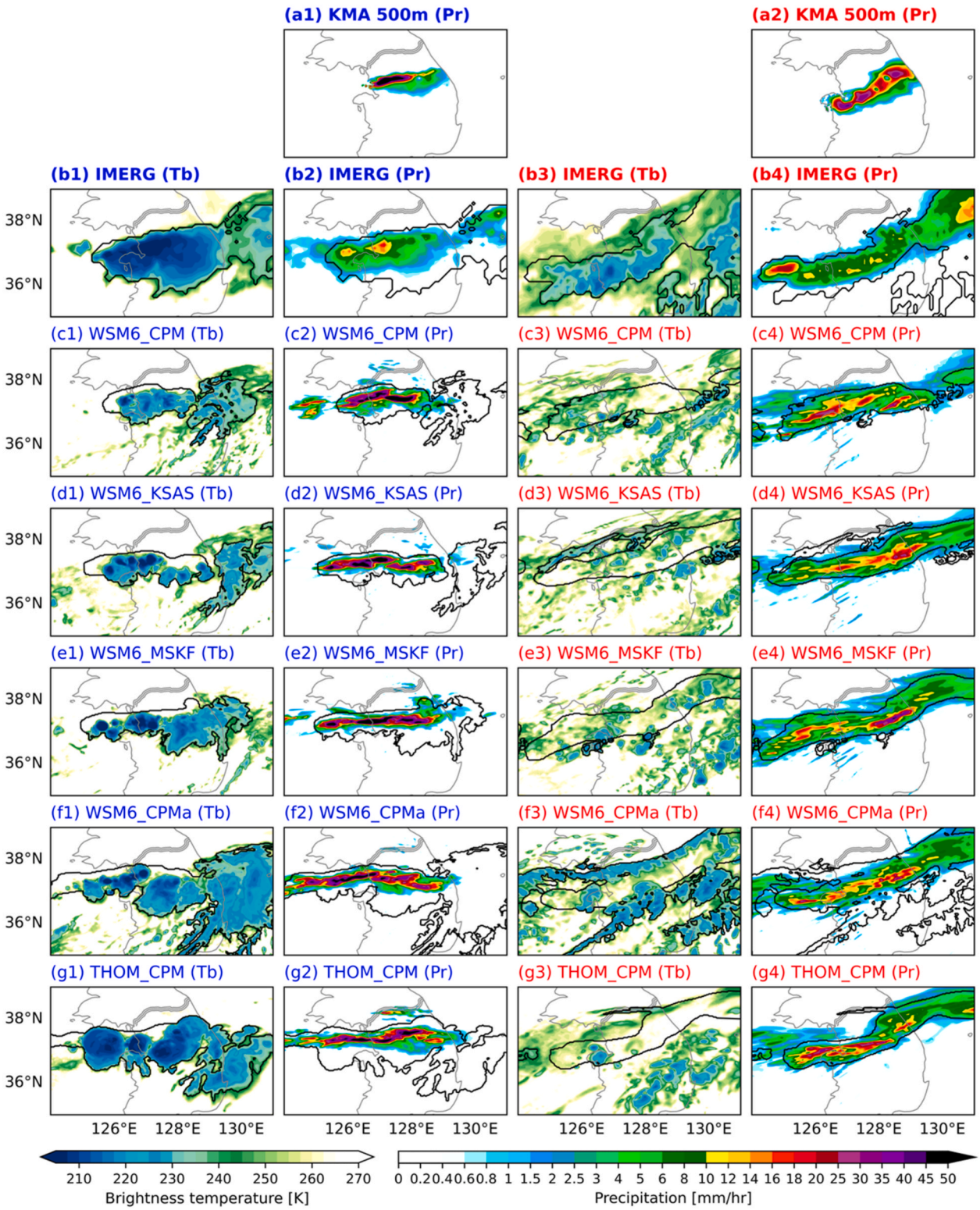


Fig. 7. Brightness temperature (T_b), precipitation (Pr), and MCS extent for the narrow and broad cases. The first and second columns correspond to the narrow case at 14:30 UTC on 8 August 2022, while the third and fourth columns correspond to the broad case at 17:30 UTC on 9 August 2022, consistent with Fig. 5. Panels (a1) and (a2) show the spatial distribution of hourly precipitation over land from the KMA 500 m dataset for the narrow and broad cases, respectively. In all panels, black contours outline the MCS extent identified by the tracking algorithm for each simulation.

rainfall is associated with convective elements not captured within the tracked MCS area. This pattern also supports the tendency of WSM6 to underestimate cloud area, so that a substantial portion of deep convection is classified as non-MCS rather than MCS convection.

4. Discussion

This study provides a process-oriented evaluation of how microphysics configuration and convection treatment shape mesoscale convective systems and unprecedented extreme rainfall during the

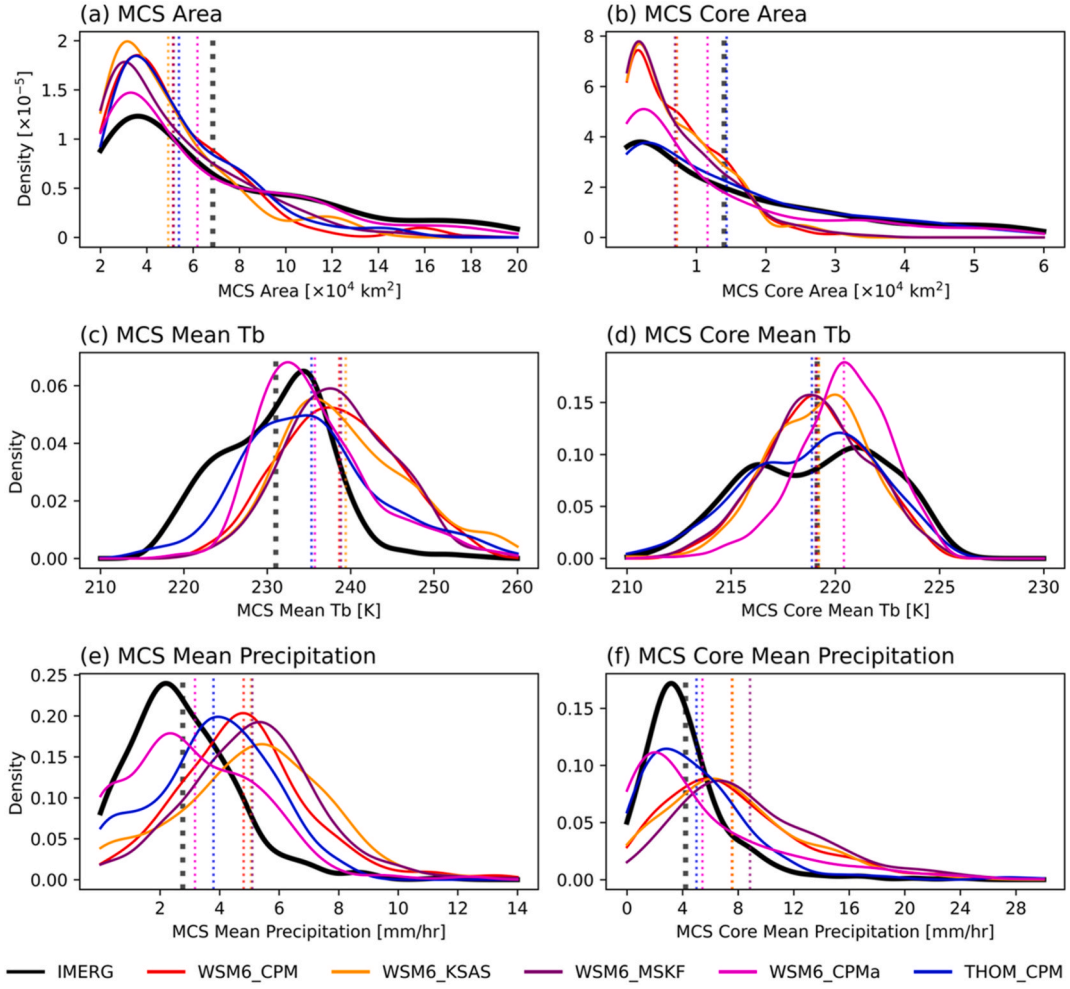


Fig. 8. Kernel Density Estimations (KDEs) of tracked MCS characteristics from each simulation, shown together with IMERG. Each panel shows the probability density of a specific MCS property, and the dashed line indicates the mean value for each simulation and IMERG.

August 2022 event over South Korea. Using WRF simulations at 3 km resolution with multiple combinations of single- and double-moment microphysics, optional scale-aware convection, and hydrometeor parameter adjustments, we diagnose the impacts of these model configurations on the spatial pattern and intensity of rainfall, major MCS properties, and associated vertical mass circulation through object-based tracking and isentropic analysis.

Across all experiments, the horizontally elongated band of accumulated extreme precipitation is generally well reproduced, but the location and magnitude of hourly precipitation vary markedly among the simulations, leading to pronounced differences in the organization of MCSs. The default WSM6 configuration favors very small, intensely precipitating cores with warm, confined anvils, substantial rainfall and strong overturning that extends outside of the tracked MCSs. In contrast, the ice-enhanced WSM6 and the Thompson scheme generate larger MCS cores, more horizontally extensive cold anvils, cooler cloud tops, and lower mean rain rates, yielding vertical mass-flux profiles that more closely resemble top-heavier MCSs seen in previous studies (Yuan and Houze, 2010; Feng et al., 2018). In WSM6, stronger conversion from ice to other hydrometeor species and fast fallout of ice confine upper-level condensate, maintaining warmer, smaller anvils and supporting intense, localized cores and strong overturning outside the tracked MCSs, whereas the enhanced ice retention and double-moment configuration redistribute condensate into broader anvils and induce a top-heavy overturning profile. Consistent with this behavior, Wu et al. (2013) showed that a three-ice scheme enhances convective areal coverage, precipitation intensity, and updraft and downdraft strengths while reducing stratiform coverage and rainfall. Additionally, Morrison et al. (2009) demonstrated that single-moment microphysics can produce negligible trailing stratiform precipitation compared with a double-moment scheme. Feng et al. (2018) further reported that differing hydrometeor representations across schemes lead to systematic changes in MCS upper-level cloud shields, precipitation areas, convective feature dimensions, and the convective–stratiform partitioning. Taken together, these results suggest that, for this specific case, microphysics scheme choice and hydrometeor representation can be influential when assessing MCS behavior, and can substantially modify simulated MCS size, rainfall distribution, and the overturning patterns between MCS and non-MCS regions.

On top of these microphysics-driven differences, two scale-aware convection schemes were also tested, but their influence is more modest and not consistent across microphysics schemes. In WSM6, activating the cumulus schemes moderately modulates the precipitation intensity and bulk skill metrics, whereas in the Thompson scheme, it produces negligible differences. From the perspective of MCS characteristics, WSM6 shows relatively small differences between CPM, KSAS, and MSKF compared with the larger changes introduced by CPMa, whereas in the Thompson scheme CPM and CPMa remain similar. These results indicate that, for this specific case, while microphysics and hydrometeor representation appear to exert a dominant control on simulated MCS structure and overturning, the influence of the scale-aware cumulus scheme is secondary and strongly dependent on the

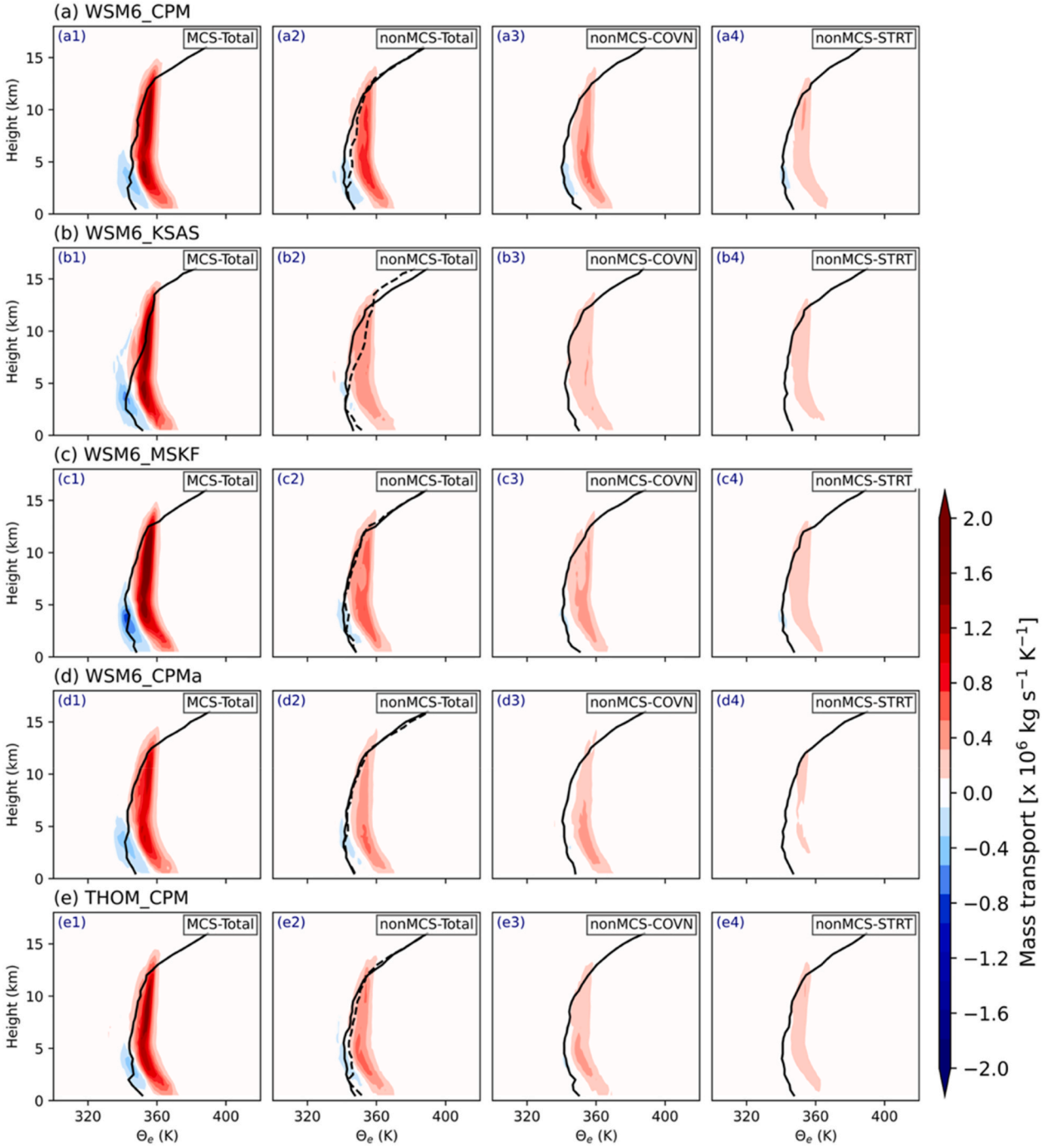


Fig. 9. Isentropic distributions of vertical mass transports for MCS and non-MCS sub-regimes. Rows (a)-(e) correspond to different simulation settings. Within each row, panel 1 shows the total mass transport associated with MCSs, whereas panels 2-4 represent the total, convective, and stratiform phases for non-MCS regimes, respectively. Solid black lines denote the horizontal-mean profiles of EPT for each phase. In the non-MCS total panel, dashed lines indicate the corresponding EPT profiles for the MCS total.

accompanying microphysics configuration.

These microphysics- and convection-driven differences and their coupling effect are particularly important in the East Asia summer monsoon environment over the Korean Peninsula, where quasi-stationary monsoon rainbands are maintained by strong moisture transport from the western North Pacific and are further modulated by complex terrain (Xu et al., 2020; Park et al., 2021). In such a moist frontal environment, the structure and evolution of the rainbands depend not only on the large-scale moisture supply but also on the vertical distribution of diabatic heating associated with embedded convection and stratiform clouds. Such heating and the associated vertical motion can modify the intensity and morphology of the fronts, thereby influencing the location and evolution of heavy rainfall in this region (Hu et al., 2021). Microphysical control of upper-level ice is therefore particularly important because it regulates the condensation and advection from convective cores and stratiform anvils. Greater retention of slowly falling ice and snow favors broader, colder cloud shields and more continuous MCS structures, whereas rapid conversion to fast-falling ice species promotes smaller, more fragmented systems (Han et al., 2019; Madhulatha et al., 2023; Mun et al., 2026).

Additionally, convective treatment strongly affects the timing of convective initiation, the placement and propagation of rainfall cores (Li et al., 2023), and their coupling can further alter the vertical partitioning of latent heating and mass flux, which can shift the system between more concentrated, core-dominated convection and more top-heavy, stratiform-rich structures (Mishra et al., 2024). Therefore, model representations of microphysics and convection govern how incoming monsoon moisture is processed, fundamentally shaping the spatial distribution, organization, and intensity of the resulting rainband.

During the August 2022 event, a narrow band of high equivalent potential temperature at mid-levels and strong vertically integrated moisture transport from the ocean toward Korea sustained deep convection along the frontal zone (Kim et al., 2025). In such a setting, configurations that confine upper-level ice and produce small, intense cores with limited stratiform area concentrate very heavy rainfall into limited areas. On the other hand, schemes that enhance anvil extent and top-heavy overturning spread condensate and rainfall over broader rainbands. Previous East Asian MCS studies have highlighted quasi-linear, front-parallel rainbands embedded in monsoon fronts and the important contribution of mid-to upper-level ice advection to seasonal monsoon rainfall (Luo et al., 2014; Zhao et al., 2020). Our results extend these regional findings by explicitly demonstrating how specific choices of microphysics and scale-aware convection can, within such a monsoon frontal environment, either reinforce a narrow, highly concentrated rainband or promote a more spatially extensive, stratiform-rich structure over the Korean Peninsula.

Despite these insights, several limitations remain. First, our analysis is based on a single extreme event over South Korea, so the conclusions should be interpreted as case-specific rather than fully general, and they may not directly apply to other types of precipitating systems or synoptic regimes. Second, the evaluation relies partly on IMERG, which tends to underestimate extreme intensities even though its combination with geostationary Tb is essential for MCS tracking over both land and ocean. Third, although we consider two widely used microphysics schemes and two scale-aware convection schemes, this still represents a limited subset of available parameterizations, and other scheme choices or tuning strategies could exhibit different sensitivities. Future work extending this process-oriented framework to multi-event ensembles, a broader range of convection-microphysics combinations, and richer observational datasets will be necessary to assess the robustness and generalizability of the mechanisms identified here.

CRediT authorship contribution statement

Dabeen Song: Writing – original draft, Visualization, Validation, Software, Methodology, Investigation, Formal analysis, Data curation. **Xingchao Chen:** Writing – review & editing, Methodology, Investigation. **Xiaoming Shi:** Writing – review & editing, Methodology, Investigation. **Hanjie Shen:** Writing – review & editing. **Daeun Kwon:** Methodology, Data curation. **Ga-Yeong Seo:** Methodology, Data curation. **Seung-Ki Min:** Writing – review & editing, Methodology, Investigation, Funding acquisition, Conceptualization. **Eun-Soon Im:** Writing – original draft, Supervision, Methodology, Investigation, Conceptualization.

Declaration of competing interest

The authors declare that they have no known competing financial interests or personal relationships that could have appeared to influence the work reported in this paper.

Acknowledgments

This study was supported by the KMA Research and Development Program under Grant RS-2024-00403386. D. Song was supported by the Hong Kong Ph.D. Fellowship Scheme from the Hong Kong Research Grants Council.

Appendix A. Supplementary data

Supplementary data to this article can be found online at https://doi.org/10.1016/j.wace.2026.100969.

Data availability

Data will be made available on request.

References

Bao, J.-W., Michelson, S.A., Grell, E.D., 2019. Microphysical process comparison of three microphysics parameterization schemes in the WRF model for an idealized squall-line case study. https://doi.org/10.1175/MWR-D-18-0249.1.

Chen, X., Leung, L.R., Feng, Z., Song, F., 2022. Crucial role of mesoscale convective systems in the vertical mass, water, and energy transports of the South Asian summer monsoon. https://doi.org/10.1175/JCLI-D-21-0124.1.

Chen, X., Leung, L.R., Feng, Z., Song, F., Yang, Q., 2021. Mesoscale convective systems dominate the energetics of the South Asian summer monsoon onset. Geophys. Res. Lett. 48, e2021GL094873. https://doi.org/10.1029/2021GL094873.

Chen, X., Leung, L.R., Feng, Z., Yang, Q., 2023. Environmental controls on MCS lifetime rainfall over tropical Oceans. Geophys. Res. Lett. 50, e2023GL103267. https://doi.org/10.1029/2023GL103267.

Chen, X., Pauluis, O.M., Zhang, F., 2018. Atmospheric overturning across multiple scales of an MJO event during the CINDY/DYNAMO campaign. https://doi.org/10.1175/JAS-D-17-0060.1.

Da Silva, N.A., Webber, B.G.M., Matthews, A.J., Feist, M.M., Stein, T.H.M., Holloway, C. E., Abdullah, M.F.A.B., 2021. Validation of GPM IMERG extreme precipitation in the maritime continent by station and radar data. Earth Space Sci. 8, e2021EA001738. https://doi.org/10.1029/2021EA001738.

Deng, A., Stauffer, D.R., 2006. On improving 4-km mesoscale model simulations. J. Appl. Meteorol. Climatol. 45 (1), 361–381. https://doi.org/10.1175/JAM2341.

Falk, N.M., Igel, A.L., Igel, M.R., 2019. The relative impact of ice fall speeds and microphysics parameterization complexity on supercell evolution. https://doi.org/10.1175/MWR-D-18-0417.1.

Fan, J., Han, B., Varble, A., Morrison, H., North, K., Kollias, P., Chen, B., Dong, X., Giangrande, S.E., Khain, A., Lin, Y., Mansell, E., Milbrandt, J.A., Stenz, R., Thompson, G., Wang, Y., 2017. Cloud-resolving model intercomparison of an MC3E squall line case: part I—Convective updrafts. JGR Atmospheres 122, 9351–9378. https://doi.org/10.1002/2017JD026622.

Feng, Z., Hardin, J., Barnes, H.C., Li, J., Leung, L.R., Varble, A., Zhang, Z., 2023. PyFLEXTRKR: a flexible feature tracking Python software for convective cloud analysis. Geosci. Model Dev. 16, 2753–2776. https://doi.org/10.5194/gmd-16-2753-2023.

Feng, Z., Houze, R.A., Leung, L.R., Song, F., Hardin, J.C., Wang, J., Gustafson, W.I., Homeyer, C.R., 2019. Spatiotemporal characteristics and large-scale environments of mesoscale convective systems east of the rocky Mountains. https://doi.org/10.1175/JCLI-D-19-0137.1.

Feng, Z., Leung, L.R., Houze Jr., R.A., Hagos, S., Hardin, J., Yang, Q., Han, B., Fan, J., 2018. Structure and evolution of mesoscale convective systems: sensitivity to cloud microphysics in convection-permitting simulations over the United States. J. Adv. Model. Earth Syst. 10, 1470–1494. https://doi.org/10.1029/2018MS001305.

Feng, Z., Leung, L.R., Liu, N., Wang, J., Houze Jr, R.A., Li, J., Hardin, J.C., Chen, D., Guo, J., 2021. A global high-resolution mesoscale convective system database using satellite-derived cloud tops, surface precipitation, and tracking. J. Geophys. Res. Atmos. 126, e2020JD034202. https://doi.org/10.1029/2020JD034202.

Fosser, G., Gaetani, M., Kendon, E.J., Adinolfi, M., Ban, N., Belušić, D., Caillaud, C., Careto, J.A.M., Coppola, E., Demory, M.-E., de Vries, H., Dobler, A., Feldmann, H., Goergen, K., Lenderink, G., Pichelli, E., Schär, C., Soares, P.M.M., Somot, S., Tölle, M.H., 2024. Convection-permitting climate models offer more certain extreme rainfall projections. npj Clim. Atmos. Sci. 7, 51. https://doi.org/10.1038/s41612-024-00600-w.

Fosser, G., Kendon, E.J., Stephenson, D., Tucker, S., 2020. Convection-permitting models offer promise of more certain extreme rainfall projections. Geophys. Res. Lett. 47, e2020GL088151. https://doi.org/10.1029/2020GL088151.

Grasso, L., Lindsey, D.T., Sunny Lim, K.-S., Clark, A., Bikos, D., Dembek, S.R., 2014. Evaluation of and suggested improvements to the WSM6 microphysics in WRF-ARW using synthetic and observed GOES-13 imagery. Mon. Weather Rev. 142, 3635–3650. https://doi.org/10.1175/MWR-D-14-00005.1.

Grell, G.A., Freitas, S.R., 2014. A scale and aerosol aware stochastic convective parameterization for weather and air quality modeling. Atmos. Chem. Phys. 14, 5233–5250. https://doi.org/10.5194/acp-14-5233-2014.

Han, B., Fan, J., Varble, A., Morrison, H., Williams, C.R., Chen, B., Dong, X., Giangrande, S.E., Khain, A., Mansell, E., Milbrandt, J.A., Shpund, J., Thompson, G., 2019. Cloud-Resolving model intercomparison of an MC3E squall line case: part II. Stratiform precipitation properties. JGR Atmospheres 124, 1090–1117. https://doi.org/10.1029/2018JD029596.

Hersbach, H., Bell, B., Berrisford, P., Hirahara, S., Horányi, A., Muñoz-Sabater, J., Nicolas, J., Peubey, C., Radu, R., Schepers, D., Simmons, A., Soci, C., Abdalla, S.,

Abellan, X., Balsamo, G., Bechtold, P., Biavati, G., Bidlot, J., Bonavita, M., De Chiara, G., Dahlgren, P., Dee, D., Diamantakis, M., Dragani, R., Flemming, J., Forbes, R., Fuentes, M., Geer, A., Haimberger, L., Healy, S., Hogan, R.J., Hólm, E., Janisková, M., Keeley, S., Laloyaux, P., Lopez, P., Lupu, C., Radnoti, G., de Rosnay, P., Rozum, I., Vamborg, F., Villaume, S., Thépaut, J.-N., 2020. The ERA5 global reanalysis. Q. J. R. Meteorol. Soc. 146, 1999–2049. https://doi.org/10.1002/qj.3803.

Hiraga, Y., Watanabe, S., Yamashita, T., Takizawa, H., 2025. Climate change effects on Probable Maximum Precipitation (PMP) of mesoscale convective systems: model-based estimation and large ensemble-based frequency analysis. J. Hydrol. 661, 133724. https://doi.org/10.1016/j.jhydrol.2025.133724.

Hohenegger, C., Brockhaus, P., Schär, C., 2008. Towards climate simulations at cloud-resolving scales. metz 17, 383–394. https://doi.org/10.1127/0941-2948/2008/0303.

Hong, S.-Y., Lim, L., 2006. The WRF single–moment 6–class microphysics scheme (WSM6). J. Korean Meteorol. Soc. 42, 129–151.

Houze Jr., R.A., 2004. Mesoscale convective systems. Rev. Geophys. 42. https://doi.org/10.1029/2004RG000150.

Houze, R.A., 2018. 100 years of research on mesoscale convective systems. https://doi.org/10.1175/AMSMONOGRAPHS-D-18-0001.1.

Hu, Y., Deng, Y., Lin, Y., Zhou, Z., Cui, C., Dong, X., 2021. Dynamics of the spatiotemporal morphology of Mei-yu fronts: an initial survey. Clim. Dyn. 56, 2715–2728. https://doi.org/10.1007/s00382-020-05619-2.

Huang, Y., Wang, Y., Xue, L., Wei, X., Zhang, L., Li, H., 2020. Comparison of three microphysics parameterization schemes in the WRF model for an extreme rainfall event in the coastal metropolitan city of Guangzhou, China. Atmos. Res. 240, 104939. https://doi.org/10.1016/j.atmosres.2020.104939.

Huffman, G.J., Stocker, E.F., Bolvin, D.T., Nelkin, E.J., Tan, J., 2024. GPM IMERG Final Precipitation L3 1 day 0.1 degree x 0.1 degree V07. https://doi.org/10.5065/7DE2-M746.

Jeong, J.-H., Lee, D.-I., Wang, C.-C., Han, I.-S., 2016. Characteristics of mesoscale-convective-system-produced extreme rainfall over southeastern South Korea: 7 July 2009. Nat. Hazards Earth Syst. Sci. 16, 927–939. https://doi.org/10.5194/nhess-16-927-2016.

Jeworrek, J., West, G., 2019. Evaluation of cumulus and microphysics parameterizations in WRF across the convective gray Zone. https://doi.org/10.1175/WAF-D-18-0178.1.

Kendon, E.J., Ban, N., Roberts, N.M., Fowler, H.J., Roberts, M.J., Chan, S.C., Evans, J.P., Fosser, G., Wilkinson, J.M., 2017. Do convection-permitting regional climate models improve projections of future precipitation change? https://doi.org/10.1175/BAMS-D-15-0004.1.

Kim, H.-A., Ho, C.-H., Kim, J., Seo, E.-K., Park, S.K., 2025. Observational study of a quasi-stationary mesoscale convective system during extreme rainfall on 8 August 2022 in Korea. Atmos. Res. 325, 108159. https://doi.org/10.1016/j.atmosres.2025.108159.

Kim, H.W., Lee, D.K., 2006. An observational Study of mesoscale convective systems with heavy rainfall over the Korean peninsula. Weather Forecast. 21, 125–148. https://doi.org/10.1175/WAF912.1.

Kim, K.-B., Kim, K., Lee, G., Lim, K.-S.S., 2024. Effects of parameters defining the characteristics of raindrops in the cloud microphysics parameterization on the simulated summer precipitation over the Korean peninsula. Atmosphere 34, 305–317. https://doi.org/10.14191/ATMOS.2024.34.3.305 (in Korean).

KMA, 2023. Abnormal climate report 2022. Korea Meteorological Administration Rep 167 (in Korean).

Ko, J.-S., Lim, K.-S.S., Kim, K., Lee, G., Thompson, G., Berne, A., 2022. Simulated microphysical properties of winter storms from bulk-type microphysics schemes and their evaluation in the Weather Research and Forecasting (v4.1.3) model during the ICE-POP 2018 field campaign. Geosci. Model Dev. 15, 4529–4553. https://doi.org/10.5194/gmd-15-4529-2022.

Kwon, D., Seo, G.-Y., Min, S.-K., Son, S.-W., Ryu, Y.-H., Im, E.-S., Cha, D.-H., Kim, J.-U., Byun, Y.-H., Boo, K.-O., 2025. Synoptic systems influence the effectiveness of spectral nudging in high-resolution simulations of extreme precipitation. npj Clim. Atmos. Sci. 8, 339. https://doi.org/10.1038/s41612-025-01224-4.

Kwon, Y.C., Hong, S.-Y., 2017. A mass-flux cumulus parameterization scheme across gray-zone resolutions. Mon. Weather Rev. 145, 583–598. https://doi.org/10.1175/MWR-D-16-0034.1.

Lenderink, G., van Meijgaard, E., 2008. Increase in hourly precipitation extremes beyond expectations from temperature changes. Nat. Geosci. 1, 511–514. https://doi.org/10.1038/ngeo262.

Li, F., Rosa, D., Collins, W.D., Wehner, M.F., 2012. "Super-parameterization": a better way to simulate regional extreme precipitation? J. Adv. Model. Earth Syst. 4. https://doi.org/10.1029/2011MS000106.

Li, P., Muetzelfeldt, M., Schiemann, R., Chen, H., Li, J., Furtado, K., Zhuang, M., 2023. Sensitivity of simulated mesoscale convective systems over East Asia to the treatment of convection in a high-resolution GCM. Clim. Dyn. 60, 2783–2801. https://doi.org/10.1007/s00382-022-06471-2.

Li, Z., Tang, G., Kirstetter, P., Gao, S., Li, J.-L.F., Wen, Y., Hong, Y., 2022. Evaluation of GPM IMERG and its constellations in extreme events over the conterminous United States. J. Hydrol. 606, 127357. https://doi.org/10.1016/j.jhydrol.2021.127357.

Lim, K.-S.S., 2020. The effects of mass-size relationship for snow on the simulated surface precipitation. J. Korean Earth Sci. Soc. 41, 1–18. https://doi.org/10.5467/JKESS.2020.41.1.1 (in Korean).

Liu, D., Yang, B., Zhang, Y., Qian, Y., Huang, A., Zhou, Y., Zhang, L., 2018. Combined impacts of convection and microphysics parameterizations on the simulations of precipitation and cloud properties over Asia. Atmos. Res. 212, 172–185. https://doi.org/10.1016/j.atmosres.2018.05.017.

Luo, Y., Gong, Y., Zhang, D.-L., 2014. Initiation and organizational modes of an extreme-rain-producing mesoscale convective System along a Mei-Yu front in east China. https://doi.org/10.1175/MWR-D-13-00111.1.

Madhulatha, A., Dudhia, J., Park, R.-S., Bhan, S.C., Mohapatra, M., 2023. Effect of single and double moment microphysics schemes and change in cloud condensation nuclei, latent heating rate structure associated with severe convective System over Korean peninsula. Atmosphere 14, 1680. https://doi.org/10.3390/atmos14111680.

Mishra, A.K., Jangir, B., Khain, P., Strobach, E., 2024. Characteristics of the Mediterranean Cyclone IANOS in convection-permitting simulations: unraveling model sensitivity to microphysics and cumulus parameterization. JGR Atmospheres 129, e2024JD041637. https://doi.org/10.1029/2024JD041637.

Molinari, J., Dudek, M., 1992. Parameterization of Convective Precipitation in Mesoscale Numerical Models: a Critical Review.

Morrison, H., Thompson, G., Tatarskii, V., 2009. Impact of cloud microphysics on the development of trailing stratiform precipitation in a simulated squall line: comparison of One- and two-moment schemes. https://doi.org/10.1175/2008MWR2556.1.

Mun, T., Cha, D., Hong, S., Dudhia, J., 2026. Sensitivity of East Asian meso- β -Scale convective systems identification to microphysical processes in a convection-permitting model. JGR Atmospheres 131, e2026JD046317. https://doi.org/10.1029/2026JD046317.

Mun, T., Park, H., Park, J., Cha, D., Lee, M., Son, S., Min, S., 2025. Spatiotemporal characteristics of mesoscale convective systems over East Asian monsoon Region simulated by a convection-permitting model. JGR Atmospheres 130, e2025JD044820. https://doi.org/10.1029/2025JD044820.

Park, C., Kang, M.-J., Hwang, J., Cho, H.-O., Kim, S., Son, S.-W., 2024. Multiscale drivers of catastrophic heavy rainfall event in early August 2022 in South Korea. Weather Clim. Extrem. 44, 100681. https://doi.org/10.1016/j.wace.2024.100681.

Park, C., Son, S.-W., Ham, Y.-G., Kim, J., Cha, D.-H., Chang, E.-C., Lee, G., Kug, J.-S., Lee, W.-S., Lee, Y.-Y., Lee, H.C., Lim, B., 2021. Record-breaking summer rainfall in South Korea in 2020: synoptic characteristics and the role of large-scale circulations. https://doi.org/10.1175/MWR-D-21-0051.1.

Pauluis, O.M., Mrowiec, A.A., 2013. Isentropic analysis of convective motions. https://doi.org/10.1175/JAS-D-12-0205.1.

Prein, A.F., Langhans, W., Fosser, G., Ferrone, A., Ban, N., Goergen, K., Keller, M., Tölle, M., Gutjahr, O., Feser, F., Brisson, E., Kollet, S., Schmidli, J., van Lipzig, N.P. M., Leung, R., 2015. A review on regional convection-permitting climate modeling: demonstrations, prospects, and challenges. Rev. Geophys. 53, 323–361. https://doi.org/10.1002/2014RG000475.

Qian, Y., Yan, H., Hou, Z., Johannesson, G., Klein, S., Lucas, D., Neale, R., Rasch, P., Swiler, L., Tannahill, J., Wang, H., Wang, M., Zhao, C., 2015. Parametric sensitivity analysis of precipitation at global and local scales in the community atmosphere model CAM5. J. Adv. Model. Earth Syst. 7, 382–411. https://doi.org/10.1002/2014MS000354.

Randall, D., Khairoutdinov, M., Arakawa, A., Grabowski, W., 2003. Breaking the Cloud Parameterization Deadlock. https://doi.org/10.1175/BAMS-84-11-1547.

Schumacher, R.S., Johnson, R.H., 2005. Organization and environmental properties of extreme-rain-producing mesoscale convective systems. https://doi.org/10.1175/MWR2899.1.

Skamarock, W.C., Klemp, J.B., Dudhia, J., Gill, D.O., Liu, Z., Berner, J., Wang, W., Powers, J.G., Duda, M.G., Barker, D.M., Huang, X.-Y., 2019. A Description of the Advanced Research WRF Model Version 4.

Stergiou, I., Traka, N., Kaskaoutis, D.G., Tagaris, E., Sotiropoulou, R.-E.P., 2025. Do the use of a convection scheme in the convective "gray zone" and the increase in spatial resolution enhance the WRF's precipitation predictive capability? Theor. Appl. Climatol. 156, 196. https://doi.org/10.1007/s00704-025-05415-0.

Thompson, G., Field, P.R., Rasmussen, R.M., Hall, W.D., 2008. Explicit forecasts of winter precipitation using an improved bulk microphysics scheme. Part II: implementation of a new snow parameterization. https://doi.org/10.1175/2008MWR2387.1.

Tokay, A., Short, D.A., 1996. Evidence from Tropical Raindrop Spectra of the Origin of Rain from Stratiform versus Convective Clouds.

Tupsoundare, M., Deshpande, S.M., Feng, Z., Das, S.K., Deshpande, M., Hanmante, H., 2025. Spatiotemporal variations in the characteristics of mesoscale convective systems over Indian monsoon Zone. J. Geophys. Res. Atmos. 130, e2024JD042344. https://doi.org/10.1029/2024JD042344.

Van Weverberg, K., Vogelmann, A.M., Lin, W., Luke, E.P., Cialella, A., Minnis, P., Khaiyer, M., Boer, E.R., Jensen, M.P., 2013. The role of cloud microphysics parameterization in the simulation of mesoscale convective system clouds and precipitation in the tropical Western Pacific. J. Atmos. Sci. 70, 1104–1128. https://doi.org/10.1175/JAS-D-12-0104.1.

White, B., Gryspeerdt, E., Stier, P., Morrison, H., Thompson, G., Kipling, Z., 2017. Uncertainty from the choice of microphysics scheme in convection-permitting models significantly exceeds aerosol effects. Atmos. Chem. Phys. 17, 12145–12175. https://doi.org/10.5194/acp-17-12145-2017.

Wu, D., Dong, X., Xi, B., Feng, Z., Kennedy, A., Mullendore, G., Gilmore, M., Tao, W.-K., 2013. Impacts of microphysical scheme on convective and stratiform characteristics in two high precipitation squall line events. J. Geophys. Res. Atmos. 118 (11). https://doi.org/10.1002/jgrd.50798, 119-11,135.

Xu, Z., Chen, J., Jin, Z., Li, H., Chen, F., 2020. Assessment of the forecast skill of multiphysics and multistochastic methods within the GRAPES regional ensemble prediction system in the East Asian monsoon Region. https://doi.org/10.1175/WAF-D-19-0021.1.

Yuan, J., Houze, R.A., 2010. Global variability of mesoscale convective System anvil structure from A-Train satellite data. https://doi.org/10.1175/2010JCLI3671.1.

Zhang, M., Xie, S., Feng, Z., Terai, C.R., Lin, W., Tao, C., Chen, C.-C.-J., Fan, J., Golaz, J.-C., Leung, L.R., Richter, J.H., Shan, Y., Song, X., Tang, Q., Zhang, G.J., 2024. Mesoscale convective systems represented in high resolution E3SMv2 and impact of new cloud and convection parameterizations. J. Geophys. Res. Atmos. 129, e2024JD040828. https://doi.org/10.1029/2024JD040828.

Zhao, Y., Liu, C., Wang, Y., Moncrieff, M.W., 2020. Quasi-stationary extreme rain produced by mesoscale convective system on the Mei-Yu front. Meteorol. Atmos. Phys. 132, 721–742. https://doi.org/10.1007/s00703-019-00717-1.

Zheng, Y., Alapaty, K., Herwehe, J.A., Del Genio, A.D., Niyogi, D., 2016. Improving high-resolution weather forecasts using the weather research and forecasting (WRF) model with an updated kain–fritsch scheme. Mon. Weather Rev. 144, 833–860. https://doi.org/10.1175/MWR-D-15-0005.1.

Zhu, H., Chen, S., Li, Z., Gao, L., Li, X., Zhu, H., Chen, S., Li, Z., Gao, L., Li, X., 2022. Comparison of satellite precipitation products: IMERG and GSMaP with rain gauge observations in Northern China. Remote Sens. 14. https://doi.org/10.3390/rs14194748.